# Effect of Different Synthesis Methods on the Textural Properties of Calcium Tungstate (CaWO₄) and Its Catalytic Properties in the Toluene Oxidation

*Lorena Dariane da Silva Alencar[a]\* [iD], Naiara Arantes Lima[a], Alexandre Mesquita[b], Luiz Fernando*

*Dias Probst[c], Daniel Carreira Batalha[d], Marcelo Gonçalves Rosmaninho[d], Humberto Vieira Fajardo[d],*

*Rosana Balzer[e], Maria Inês Basso Bernardi[a]*

[a]*Instituto de Física de São Carlos, Universidade de São Paulo - USP, 13563-120, São Carlos, SP, Brasil*
[b]*Departamento de Física, Instituto de Geociências e Ciências Exatas, Universidade Estadual Paulista - Unesp, 13506-900, Rio Claro, SP, Brasil*
[c]*Departamento de Química, Universidade Federal de Santa Catarina - UFSC, 88040-900, Florianópolis, SC, Brasil*
[d]*Departamento de Química, Instituto de Ciências Exatas e Biológicas, Universidade Federal de Ouro Preto - UFOP, 35400-000, Ouro Preto, MG, Brasil*
[e]*Departamento de Engenharias e Exatas, Universidade Federal do Paraná - UFPR, 85950-000, Palotina, PR, Brasil*

Calcium tungstate (CaWO₄) crystals were prepared by microwave-assisted hydrothermal (MAH) and polymeric precursor methods (PPM). These crystals were structurally characterized by X-ray diffraction (XRD), N₂ adsorption, X-ray absorption near edge spectroscopy (XANES) and extended X-ray absorption fine structure (EXAFS) measurements. The morphology and size of these crystals were observed by field emission scanning electron microscopy (FE-SEM). Their optical properties were investigated by ultraviolet visible (UV-Vis) absorption and photoluminescence (PL) measurements. Moreover, these materials were employed as catalysts towards gas phase toluene oxidation reaction. XRD indicates the purity of materials for both preparation methods and MAH process produced crystalline powders synthesized at lower temperatures and shorter processing time compared to the ones prepared by PPM. FE-SEM images showed particles with rounded morphology and particles in clusters dumbbells-like shaped. PL spectra exhibit a broad band covering the visible electromagnetic spectrum in the range of 360 to 750 nm. XANES and EXAFS results show that preparation method does not introduce high disorders into the structure, however the H₂-TPR results indicated that the catalyst reducibility is affected by the preparation method of the samples.

**Keywords:** *CaWO₄, Toluene, H₂-TPR, XANES, EXAFS.*

## 1. Introduction

Calcium tungstate, with formula CaWO₄, presents its primitive cell formed by ionic groups $Ca^{2+}$ and $WO_4^{2-}$ characterized by an arrangement of $[CaO_8]$ in a deltahedral coordination and a $[WO_4]$ tetrahedral coordination clusters[1]. It is a versatile material that exhibit thermal and optical properties[2-4] well known in the literature. Catalytic properties of calcium compounds have been studied. For example they have potential applications in catalysis for water oxidation[5-6], for ethanolysis of vegetable oils[7-8] and for $CO_2$ and steam carbon gasifications[9-10].

Several synthesis methods have been developed to obtain CaWO₄ crystals: co-precipitation, solvothermal, microwave-hydrothermal[11-12], electrochemical[13], aiming to reduce the processing time and temperatures encountered in traditional methods, such as an oxide mixture or solid state reaction. In this paper, CaWO₄ powders were synthesized

by microwave-assisted hydrothermal (MAH) method and polymeric precursor method (PPM). PPM allows to obtain high-purity homogeneous systems at the molecular scale due the immobilization of the metal cations in a polymeric networks, which can be annealed at relatively low temperatures (700 ºC)[14-15]. Microwave-assisted hydrothermal method is able to synthesize inorganic materials, such as tungstates, because the high frequency of the electromagnetic radiation promotes a rapid heating accelerating the chemical reactions[16-18].

In this work, we present the preparation of CaWO₄ samples, through MAH and PPM methods, their characterization and catalytic properties towards gas phase toluene oxidation reaction. The emission of a volatile organic compound (VOC), such as toluene, can be controlled using destruction methods in which they are converted into carbon dioxide and water. In this regard, catalytic oxidation has been one of the most efficient and promising technologies for abatement of
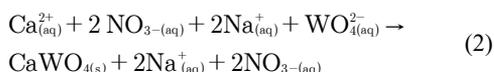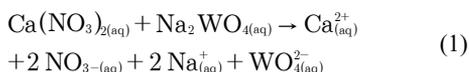
these compounds, mainly because of the high degradation efficiency, even in effluents with low concentrations of VOCs, and low energy and costs involved[17,19-21]. The choice of the suitable catalyst to be applied in the process is difficult due to the variety and nature of the range of mixtures of VOCs[21]. Therefore, this study aimed to contribute to the development of heterogeneous catalysts for this purpose.

## 2. Experimental

Polycrystalline $CaWO_4$ particles were synthesized by microwave-assisted by hydrothermal method (MAH) and polymeric precursor method (PPM).

### 2.1 Synthesis of $CaWO_4$ by microwave-assisted by hydrothermal (CWOH)

Stoichiometric $CaN_2O_6$-$4H_2O$ (*Sigma-Aldrich*, 99%) and $Na_2WO_4$-$2H_2O$ (*Sigma-Aldrich*, 99%) were singly dissolved in distilled water at 70 °C and then they were mixed. A desired amount of ethylene glycol (EG) (*Synth,* 99%) was dissolved in the above solution as polymeric reagent ($H_2O$:EG ratio of 5.3). The pH value of above solution was adjusted to 11 by ammonium hydroxide (*Synth*, 27%) addition in order to increase the system's hydrolysis rate. After the co-precipitation reaction (equations (1), (2)) the solution was transferred to a Teflon cup and subsequently into the autoclave; this was coupled to the domestic microwave oven (2.45 GHz, maximum power of 800 W). Processing occurred at 140°C for 30 min and the heating rate was set at 25 °C min$^{-1}$.

$$Ca(NO_3)_{2(aq)} + Na_2WO_{4(aq)} \rightarrow Ca^{2+}_{(aq)}$$
$$+ 2\,NO_{3-(aq)} + 2\,Na^+_{(aq)} + WO^{2-}_{4(aq)} \tag{1}$$

$$Ca^{2+}_{(aq)} + 2\,NO_{3-(aq)} + 2Na^+_{(aq)} + WO^{2-}_{4(aq)} \rightarrow$$
$$CaWO_{4(s)} + 2Na^+_{(aq)} + 2NO_{3-(aq)} \tag{2}$$

The precipitate formed was washed several times with distilled water, it was centrifuged, and then dried around 80 °C in an oven for about 8 hours to get white powder.

### 2.2 Synthesis of $CaWO_4$ by polymeric precursor method (CWOP)

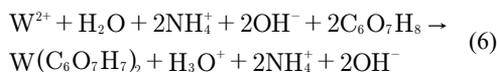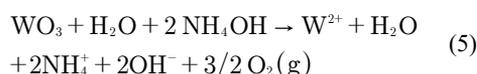To prepare $CaWO_4$ powders, $3.5 \times 10^{-2}$ mol of $H_2WO_4$ (*Aldrich*, 99%) was dissolved in 100 mL of distilled water under constant stirring and heating of approximately 70 °C then the pH of the solution was increased to $\approx 11$ by adding 10 mL of $NH_4OH$ (*Synth,* 27% in $NH_3$,) for complete dissolution of the tungstic acid. Citric acid (*Synth*, 99.5%) was dissolved in 100 mL of distilled water under the same conditions of temperature and stirring, it was added to the initial solution of tungstic acid, obtaining the tungsten citrate. After homogenization, $3.5 \times 10^{-2}$ mol of $Ca(NO_3)_2$-$4\,H_2O$ (*Sigma-Aldrich*, 99%) was diluted in

100 mL of distilled water and added to the tungsten citrate. EG in a proportion (weight) citric acid/EG of 60:40 was added to promote polyesterification of the complex (eq. (3) - (8)). The temperature was raised to 150 to 200 °C in order to promote the polyesterification reaction and evaporation of the excess water.

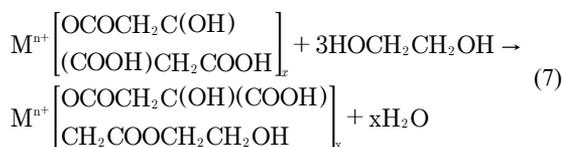The complexation of calcium with citric acid led to the following reactions:

$$Ca(NO_3)_2\,4H_2O + 2C_6O_7H_8 \rightarrow$$
$$Ca(C_6O_7H_7)_2 + 2HNO_3 + 4H_2O \tag{3}$$

forming nitric acid and water. The tungsten complexation reaction occurred as follows:

$$H_2WO_{4(aq.)} \xrightarrow{70°C} WO_3 + H_2O \tag{4}$$

$$WO_3 + H_2O + 2\,NH_4OH \rightarrow W^{2+} + H_2O$$
$$+ 2NH_4^+ + 2OH^- + 3/2\,O_2(g) \tag{5}$$

$$W^{2+} + H_2O + 2NH_4^+ + 2OH^- + 2C_6O_7H_8 \rightarrow$$
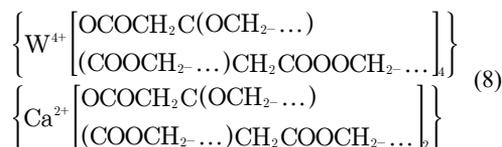$$W(C_6O_7H_7)_2 + H_3O^+ + 2NH_4^+ + 2OH^- \tag{6}$$

forming ammonium hydroxide and water.

Mixing these metallic complexes (metallic citrates) above 70 °C triggers the onset of the esterification reaction between metal citrate and ethylene glycol, as follows:

$$M^{n+}\begin{bmatrix} OCOCH_2C(OH) \\ (COOH)CH_2COOH \end{bmatrix}_x + 3HOCH_2CH_2OH \rightarrow$$
$$M^{n+}\begin{bmatrix} OCOCH_2C(OH)(COOH) \\ CH_2COOCH_2CH_2OH \end{bmatrix}_x + xH_2O \tag{7}$$

In the compounds studied here, the polyesterification reaction occurred continuously until the polymer network was formed. Based on these reactions, the following basic units can be formed in the polymeric network:

$$\left\{W^{4+}\begin{bmatrix} OCOCH_2C(OCH_{2-}\ldots) \\ (COOCH_{2-}\ldots)CH_2COOOCH_{2-}\ldots \end{bmatrix}_4\right\}$$
$$\left\{Ca^{2+}\begin{bmatrix} OCOCH_2C(OCH_{2-}\ldots) \\ (COOCH_{2-}\ldots)CH_2COOCH_{2-}\ldots \end{bmatrix}_2\right\} \tag{8}$$

The main organic compounds contained in the resin were water, ammonium hydroxide, nitric acid and polyester.

The polymer resin was annealed at 300 °C for 4 hours at a heating rate of 10 °C min$^{-1}$ in ambient atmosphere. The material obtained was deagglomerated using an agate mortar and it was annealed at 700 °C for 2 hours, at a heating rate of 10 °C min$^{-1}$ in ambient atmosphere. The molar ratio between metal cations was 1:1 and the molar ratio stoichiometry between citric acid/metal was 3:1.

### 2.3 Sample characterizations

The crystallinity of synthesized samples were characterized by powder X-ray diffraction (XRD) with a RIGAKU - ULTIMA IV X-Ray diffractometer using

Effect of Different Synthesis Methods on the Textural Properties of Calcium Tungstate (CaWO₄) and Its Catalytic Properties in the Toluene Oxidation

3

Cu-Kα (λ = 1.5406 Å) radiation for 2θ values from 20° to 80°. The morphology of the particles was investigated by scanning electron microscope (SEM; Zeiss - Sigma). UV-Visible (UV-Vis) spectroscopy was measured in the range of 200 - 900 nm (Varian Cary - 5G spectrophotometer). Photoluminescence (PL) spectra were obtained on a Monospec 27 monochromator (Thermal Jarrel-Ash) and a R446 photomultiplier (Hamatsu Photonics) compound of a lock-in SR-530 using a wavelength excitation of 350 nm generated by krypton ion laser with adjustable output power of 200 mW to 800 mW. The width of the slit used in the monochromator is 200 µm. All of the above mentioned characterization techniques were carried out at room temperature. Nitrogen adsorption-desorption measurements of obtained powders were performed at 77 K with an ASAP 2020 - MICROMERITICS adsorption apparatus. The surface areas were determined by Langmuir model in the adsorption data in a relative pressure range of 0.05-0.2. X-ray absorption near edge spectroscopy (XANES) and extended X-ray absorption fine structure (EXAFS) measurements at the W LIII-edge (10203 eV) of CaWO₄ samples were collected in transmission mode as a function of the temperature using a Si(111) channel-cut monochromator at the LNLS (National Synchrotron Light Laboratory) facility using the D04B-XAFS1 beam line. The extraction and fit of the EXAFS spectra were performed using the multi-platform applications for X-ray absorption (MAX) software package[22] and theoretical spectra were obtained using the FEFF9 code[23]. Hydrogen temperature programmed reduction (H₂-TPR) analyses were performed in a Quantachrome ChemBET-TPD/TPR, from room temperature to 1100 °C, at 10 °C min⁻¹ heating rate, using a 5%H₂/N₂ mixture (25 mL min⁻¹ flow rate) as reducing gas and about 50 mg of sample. The resulting curves were analyzed using Origin 9.0.0 software and the observed peaks were adjusted using Gaussian model.

## 2.4 Catalytic tests

The catalytic oxidation of toluene was carried out, under atmospheric pressure, in a fixed-bed tubular quartz reactor placed in an oven. The tests were performed under the following conditions: 0.11 g of catalyst, inlet toluene (>99%,Vetec) concentration 0.7 g m⁻³ in air, gas flow rate 20 cm³ min⁻¹, residence time 0.3 s, gas hourly space velocity 12000 h⁻¹ and temperature range 50-350 °C. To monitor the reaction temperature, the catalyst was placed in the middle of the reactor with thermocouples located on the top and bottom of the catalyst bed. The catalyst was previously activated in situ under air atmosphere at 250 °C for 1 h. A peristaltic pump (Minipuls 3 - Gilson®) was used to deliver the reagent feed into the reactor system. The reaction data were collected after at least 2 hours on stream at room temperature. The reactant and

product mixtures were analyzed with two in-line gas chromatographs equipped with FID and TCD detectors and an HP-5 column. The catalytic activity was expressed as the percent conversion of toluene. The conversion of the toluene was calculated as follows: $C(\%) = \frac{[Q]_{in} - [Q]_{out}}{[Q]_{in}} \times 100\%$, where C(%) = percentage of toluene conversion, $[Q]_{in}$ = input quantity and $[Q]_{out}$ = output quantity of toluene. According to the chromatograms, water and carbon dioxide were the only products detected during the experiments.

# 3. Results and Discussion

## 3.1 X-ray diffraction analyses

All the diffraction peaks in Figure 1 correspond to the reflections of tetragonal scheelite structure (space group $I4_1/a$) with CaWO₄ cell parameters $a = b = 5.243$ Å and $c = 11.376$ Å according to Inorganic Crystal Structure Database (ICSD) card N° 15586. Sharp diffraction peaks indicate the high degree of crystallinity of the powder prepared and no remarkable diffraction peak of other phases can be found in the XRD patterns. These results confirm that the MAH process produced crystalline powders synthesized at low temperatures with shorter processing time when compared to the PPM.
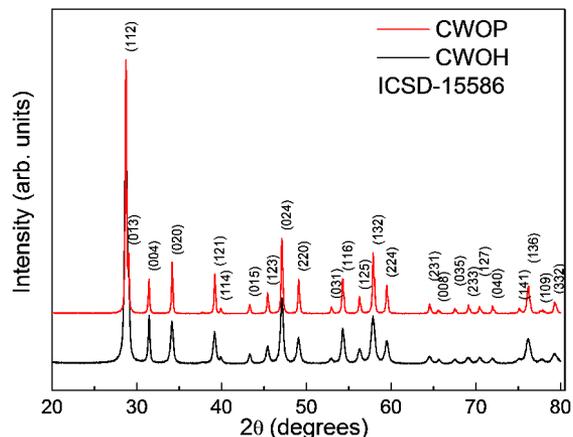


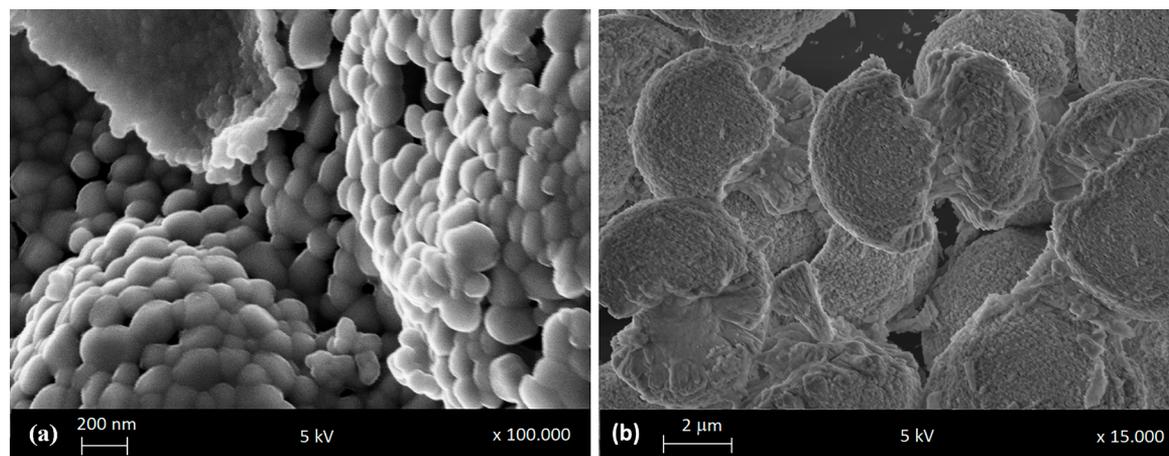**Figure 1.** XRD patterns of CWOH and CWOH powders

The crystallite sizes of the samples are determined by applying the Debye-Scherrer formula, $D = K\lambda/(\beta\cos\theta)$, where λ is the wavelength of the X-ray radiation, K is a constant taken as 0.9, β is the full width at half-maximum (FWHM) in radian of the main peak, and θ is the diffracting angle[24]. The crystallite sizes are estimated of 45 and 29 nm for CWOP and CWOH, respectively. The crystallite size is related with the processing temperature. CWOH sample was heating at 140 ºC and CWOP sample was annealed at 700 ºC. Observing Table 1, it is possible to deduce that elevating heating temperature would favor the crystallite growth[25-29].

**Table 1.** Comparative results between the crystallite size by Debye–Scherrer formula obtained in this work (*) with those published in the literature. CP = Co-precipitation, PR = Precipitation, MAH = Microwave-assisted hydrothermal, HC = Hydrothermal conventional, SR = Synthetic route, CC = Citrate complex precursor and MPP = Polymeric precursor method.

| Method | Temperature (°C) | Crystallite size (nm) | Ref. |
|--------|------------------|-----------------------|------|
| CP | 80 | 18 | [25] |
| PR | 100 | 24 | [26] |
| MAH | 140 | 29 | * |
| HC | 190 | 32 | [27] |
| SR | 500 | 33 | [28] |
| CC | 500 | 35 | [29] |
| PPM | 700 | 45 | * |

### 3.2 Field emission scanning electron microscopy analyses

FE-SEM images (Fig. 2(a.b)) show that the polycrystalline powders obtained by PPM are composed of a number of nanosized particles (Fig. 2.a). These particles are agglomerated with rounded morphology and average diameters of 100 nm. CWOH (Fig. 2.b) has particles in clusters dumbbells-like shaped. These clusters with recognizable boundaries are constructed from the highly oriented nanoparticles connected with each other during the self-assembly process[30]. The formation of such morphology was reported earlier in tungstates like $SrWO_4$, $CaWO_4$ and $BaWO_4$[30-33]. The possible formation mechanism of this morphology has been proposed by some researchers based on surfactant and polymeric agents under different experimental conditions[34].
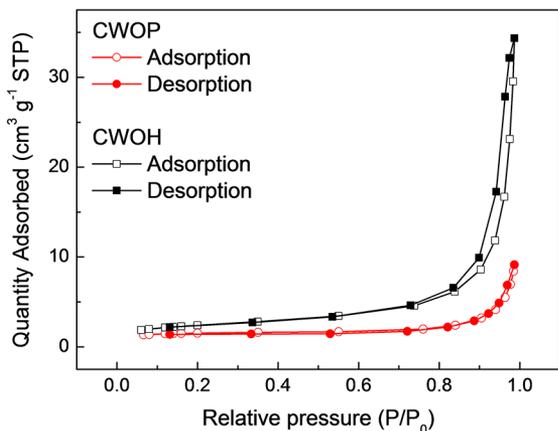
### 3.3 Nitrogen adsorption-desorption

The $N_2$ adsorption-desorption isotherms of $CaWO_4$ synthesized by PPM and MAH are shown in Fig. 3. The isotherms resemble those of type III isotherms (BDDT classification) and exhibit a H3-type hysteresis loop, which demonstrates some aggregation of plate-like crystals, yielding slit-shaped pores[35]. The Langmuir surface area of obtained samples are about 7 and 12 $m^2$ $g^{-1}$ for CWOP and CWOH samples, respectively.
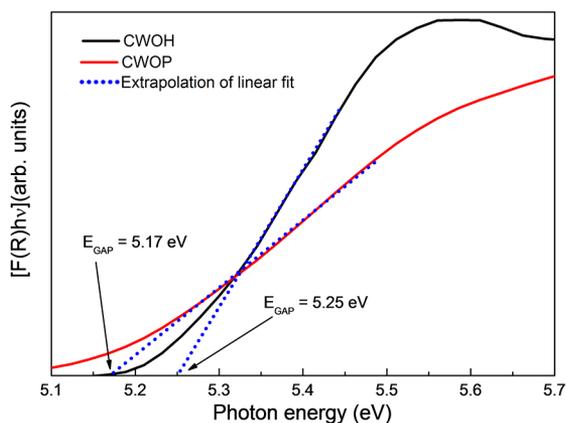
### 3.4 UV-Visible absorption measurements

UV-Vis spectroscopy measurements were performed in the diffuse reflectance mode and the optical band gap energy (Eg) was calculated by the method proposed by Kubelka- Munk for any wavelength[11,36]. The Figure 4 shows the Eg obtained and Table 2 shows the Eg values obtained in this work and values found in the literature[11,37-40]. Differences of Eg value may be related to particle morphology, type of synthesis, time and temperature of the process. All these factors result in different structural defects, such as oxygen vacancies and link distortions, which are able of promoting the formation of intermediate states of energy within the band gap[41].

According to the literature, $CaWO_4$ exhibit an optical absorption spectrum governed by direct electronic transitions, the maximum-energy states in the valence band coincide with the minimum-energy states in the conduction band[1,42]. The valence and conduction bands near the band gap are dominated mainly by contributions from molecular orbitals associated with the $WO_4^{-2}$ions[43].



**Figure 2.** FE-SEM images of (a) CWOP and (b) CWOH powders

**Table 2.** Eg values obtained in this work (*) and values found in the literature. MPP = Polymeric precursor method; MAH = Microwave-assisted hydrothermal; CP = Co precipitation; SR = Sonochemistry reaction. SPR = Solid-phase reaction.

| Method | PPM | HAM | CP | HAM | SR | PPM | SPR |
|--------|-----|-----|-----|-----|-----|-----|-----|
| Eg (eV) | 5.17 | 5.23 | 5.39 | 5.56 | 4.08 | 5.27 | 4.86 |
| Ref. | * | * | [37] | [11] | [38] | [39] | [40] |

Effect of Different Synthesis Methods on the Textural Properties of Calcium Tungstate (CaWO₄) and Its Catalytic Properties in the Toluene Oxidation

5



**Figure 3.** The $N_2$ adsorption-desorption isotherms of CaWO$_4$ synthesized by PPM and MAH



**Figure 4.** Optical band gap energy ($E_g$) calculated by the method proposed by Kubelka - Munk for any wavelength of CaWO$_4$ powders synthesized by MAH and PPM

*3.5 PL measurements*

Photoluminescence properties of the CaWO$_4$ (Fig. 5) structures were also measured. With excitation wavelength at 350 nm, PL spectra exhibit a broad band covering the visible electromagnetic spectrum in the range of 360 to 750 nm. The profile of the emission band is characteristic of processes at various levels involving the participation of several states within the band gap[16]. The materials showed green emission peaks of 492 nm e 495 nm for CaWO$_4$ prepared by PPM and MAH, respectively.

In order to evaluate the colorimetric performance of the materials, the emissions colors were analyzed using the Commission Internationale de l'Eclairage (CIE, 1964) chromaticity coordinates x;y. The inset in Figure 5 shows the CIE chromaticity diagram for the emission spectra of CWOP and CWOH under 350 nm excitation wavelength. The calculated CIE coordinates for CWOP are x = 0.26, y = 0.50 and for CWOH the coordinates are x = 0.30, y = 0.44. These coordinates are located in the green area at the diagram.
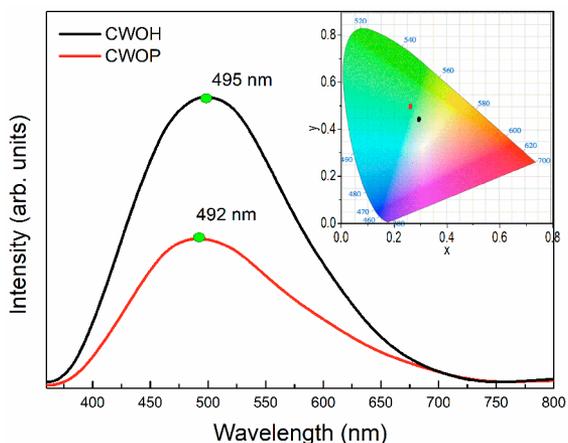


**Figure 5.** PL spectra of CaWO$_4$ powders ($\lambda_{EXC}$ = 350 nm). The maximum emission peaks are centered on 492 nm and 495 nm for CWOP and CWOH, respectively. Inset: CIE chromaticity diagram for the emission spectra of CaWO$_4$ powders

According to Cavalcante et al.[11] and Campos et al.[39], the green emission of tungstates have different interpretations. In general, two different mechanisms are responsible for the green emission spectra of CaWO$_4$ crystals: the disorder caused by [WO$_4$]$^{2-}$ complexes due to the vacancies as [WO$_3$ . V$^z_O$] (where V$^z_O$ = V$^{\bullet}_O$ or V$^{\bullet\bullet}_O$) and intrinsic slightly distorted [WO$_4$] tetrahedral in a short range in the ordered structure[31,39,44].

It is known in the literature that CaWO$_4$ samples with various morphologies exhibit different photoluminescence properties[30,45]. In this work, rounded and dumbbells-like particles showed PL emission peaks position very near, however the emission intensity was strongly influenced by the temperature of the synthesis. The material prepared by MAH (synthesized at 140 °C) have higher emission intensity when compared to the material synthesized by PPM (synthesized at 700 °C). Moreover, several factors influence the emission intensity such as the degree of aggregation and orientation between the particles, variations in particle size distribution and surface defects[19].

*3.6 X-ray absorption spectroscopy measurements*

X-ray absorption spectroscopy (XAS) is a powerful tool for the investigation of local structures and provides meaningful additional structural information on materials. Although the local structural data afforded by XAS are usually not sufficient to construct a whole structural model, they often provide valuable information about the local structural peculiarities.

Fig. 6 presents the XANES spectra at W L$_{III}$-edge for CaWO$_4$ samples and a WO$_3$ standard reference. As it can observed in this figure, XANES spectra for CAWO$_4$ powders exhibit different characteristics compared to the XANES spectrum of the reference compound (WO$_3$). In these spectra, the white line mainly derives from electron transitions from

the 2*p* 3/2 state to a vacant 5*d* state[12]. The difference between sample and reference spectra is expected because W atoms are in an octahedral environment for the $WO_3$ compound[12]. No significant change is observed in these XANES spectra as a function of the preparation method for $CaWO_4$ samples.
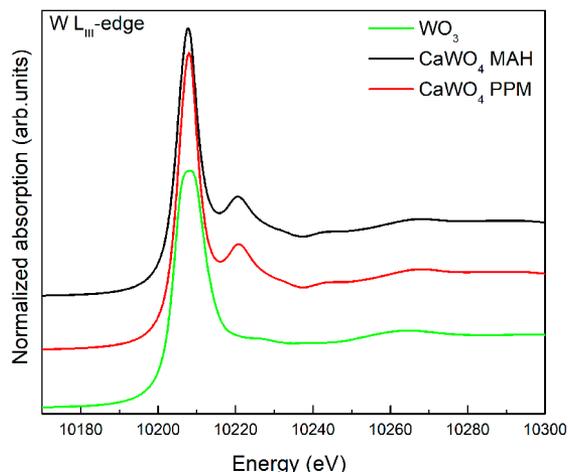


**Figure 6.** XANES spectra at W $L_{III}$-edge of $CaWO_4$ powders

EXAFS spectra at W $L_{III}$-edge were also measured in order to obtain quantitative information at local structure such as the number, position and identity of atoms surrounding the absorbing element as well as structural disorder within the coordination spheres[14]. Fig. 7 shows the modulus of $k^3$ weighted Fourier transform of $CaWO_4$ samples extracted from W $L_{III}$-edge spectra. According to the structural model calculated from the FEFF9 code and crystallographic information according to the XRD measurements, the absorber atom is surrounded by, in this order, two shells with four O atoms each, two shells with four Ca atoms each, one shell with four W atoms and three shells with four O atoms each. Thus, the more intense peak, between 1.0 and 2.0 Å in the Fourier transforms, corresponds to a single scattering interaction between the first four O atoms around the absorber atom. The single scattering interactions relative to W-Ca, W-W and W-O (beyond the first O neighbors)
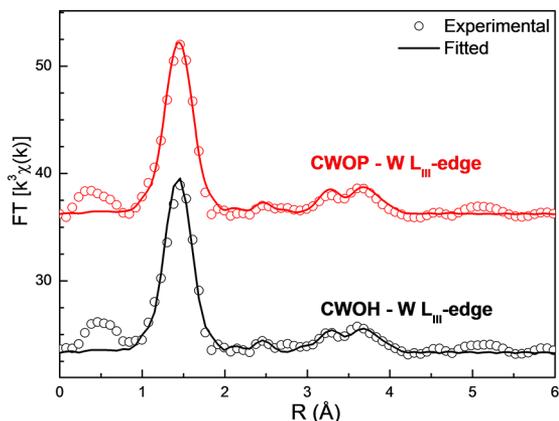


**Figure 7.** Experimental and fitted modulus of $k^3$ weighted Fourier transform for $CaWO_4$ powders at W $L_{III}$-edge. Open symbols are experimental data, and solid lines represent fittings using the parameters listed in Table 3

paths correspond the region observed between 2.0 and 5.0 Å. This region also includes multiple scattering.

Fourier transform curves were then back Fourier transformed between 1.0 and 4.0 Å to obtain the experimental EXAFS spectra to fit using a theoretical model calculated from the FEFF9 code and crystallographic information according the XRD measurements. In all fits, the number of free parameters was kept smaller than the number of independent points, which is defined as $N_{ind} = 2\Delta R\Delta k/\pi$, where $\Delta R$ is the width of the R-space filter windows and $\Delta K$ is the actual interval of the fit in the k space[46]. The reliability of the fit, determined by a quality factor (Q)[47], the interatomic distances (R) and Debye-Waller factor ($\sigma^2$) relatives to the best fits are shown in Table 3.

The results of the fits confirm the supposition that synthesis conditions do not introduce high disorders into the structure. The radial distance (R) for all shells does not change considerably as function of the preparation. Moreover, we can trace an increase of oxygen vacancies following the average coordination number (N) for the fourth and fifth O-shells, since sample prepared by PPM shows a lower coordination number in these shells. It can indicate the presence of imperfectness in the crystal lattice. As shown by FE-SEM micrographs, the average particle size is lower for these samples. Due to this, large

**Table 3.** W LIII-edge EXAFS simulation results. R is the distance from the central atom, N is the average coordination number, $\sigma^2$ the Debye–Waller factor, and Q the quality factor.

| Shell | R (Å) | | N | | $\sigma^2(10^{-2}Å^2)$ | | Q | |
|---|---|---|---|---|---|---|---|---|
| | MAH | PPM | MAH | PPM | MAH | PPM | MAH | PPM |
| W-O | 1.78(1) | 1.78(1) | 4.29(16) | 4.28(17) | 0.082(42) | 0.08(2) | | |
| W-O | 2.88(1) | 2.89(2) | 2.09(41) | 2.15(59) | | | | |
| W-Ca | 3.67(1) | 3.68(1) | 2.34(42) | 1.65(65) | | | | |
| W-Ca | 3.84(1) | 3.84(1) | 0.07(3) | 4.31(85) | | | | |
| W-W | 3.90(1) | 3.90(1) | 2.19(63) | 4.93(1.07) | 0.74(12) | 0.87(10) | 2.55 | 2.13 |
| W-O | 4.02(2) | 4.02(4) | 0.005(19) | 6.52(1.50) | | | | |
| W-O | 4.02(2) | 4.04(4) | 3.98(1.25) | 0.00(0.94) | | | | |
| W-O | 4.02(2) | 4.04(4) | 5.29(1.22) | 0.00(0.98) | | | | |

Effect of Different Synthesis Methods on the Textural Properties of Calcium Tungstate (CaWO$_4$) and Its Catalytic Properties in the Toluene Oxidation

7

amount of the atoms should be placed at the boundary of particles resulting in a lower number of neighbours[48].

## 3.7 H$_2$-TPR measurements

The H$_2$-TPR profiles for the materials are shown in the Fig. 8 and the reduction peak temperature and corresponding hydrogen consumption are listed in Table 4 bellow.

The CaWO$_4$ samples presented several reduction peaks at the H$_2$-TPR profiles, with the reduction beginning at about 250 °C for both materials. It can be observed a decreasing of the reduction temperatures for the material produced by MAH method, although the main step reduction still occurs at temperature above 1100 °C for both CWOH e CWOP produced materials. The total hydrogen consumption is larger for the CWOH sample than for CWOP. The CWOH sample shows to possess a high amount of reducible oxide, consuming 2.6 more hydrogen per mass unit than the CWOP one.

## 3.8 Catalytic activity toward toluene oxidation

Gas-phase toluene oxidation was selected as a probing reaction to evaluate the catalytic potential of the CaWO$_4$ prepared samples. The results are presented

in Fig. 9. Previously, the toluene thermal oxidation was carried out without the catalyst. Toluene conversion was negligible at low temperatures. The process started at 350 °C achieving only about 3% of conversion at 500 °C (not shown). In the presence of the catalyst, no significant toluene conversion could be observed at very low temperatures (below 100 °C). The catalysts displayed appreciable activities from 150 °C, particularly CWOH that reached almost 11% of toluene conversion. The catalysts showed a similar tendency, that is, an increase in the toluene conversion with the increase in the reaction temperature. However, it can be easily seen that CWOH showed better catalytic activity than CWOP. For example, 10% of toluene conversion was achieved at about 140 °C over CWOH, whereas the same conversion required approximately 260 °C over CWOP. Comparing the specific surface areas of both catalysts, it could be conclude that this property had only a minor influence on the catalytic activities presented, since the specific surface areas were similar. The superior performance of CWOH catalyst can be ascribed to its higher reducibility and oxygen mobility, estimated by means of H$_2$-TPR measurements, as it can be deduced
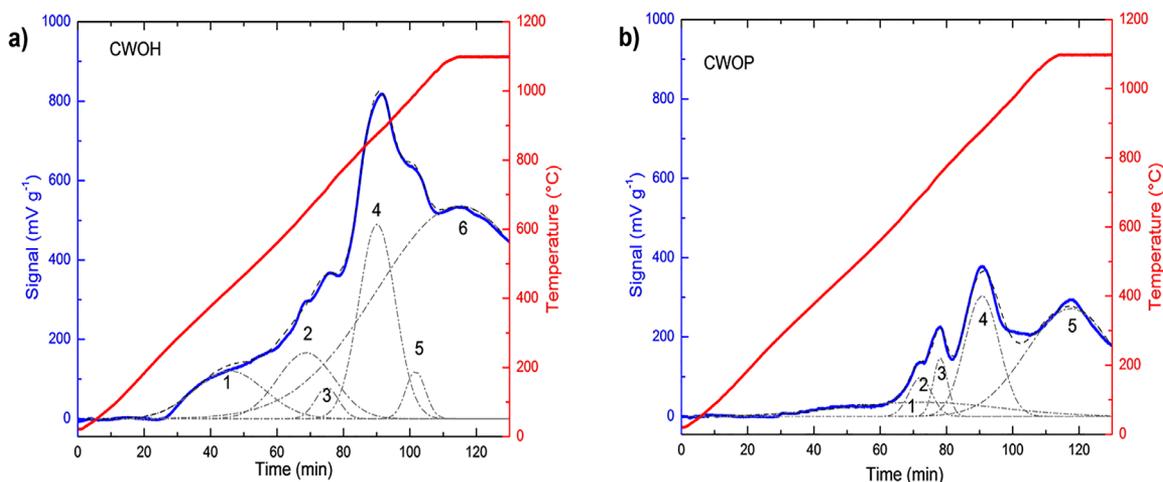


**Figure 8.** H$_2$-TPR profiles obtained for CWOH (a), and CWOP (b)

**Table 4.** Fit peak data obtained by TPR profiles of the materials produced by both MAH and PPM synthesis methods.

| Sample | Peak | Temperature (°C) | Relative Area (%) | H$_2$Consumption (mol g$^{-1}$) | |
|--------|------|------------------|-------------------|------------------|--|
| CWOH | 1 | 429 | 8 | 3.54 x10$^{-4}$ | |
| | 2 | 643 | 9 | 3.99 x10$^{-4}$ | |
| | 3 | 715 | 2 | 8.86 x10$^{-5}$ | 4.43 x10$^{-3}$ |
| | 4 | 873 | 17 | 7.53 x10$^{-4}$ | |
| | 5 | 988 | 2 | 8.86 x10$^{-5}$ | |
| | 6 | 1100 | 62 | 2.75 x10$^{-3}$ | |
| CWOP | 1 | 685 | 14 | 2.51 x10$^{-4}$ | |
| | 2 | 689 | 6 | 1.07 x10$^{-4}$ | |
| | 3 | 753 | 5 | 8.95 x10$^{-5}$ | 1.79 x10$^{-3}$ |
| | 4 | 879 | 26 | 4.65 x10$^{-4}$ | |
| | 5 | 1100 | 49 | 8.77 x10$^{-4}$ | |

from Fig. 8 and Table 4. The catalyst reducibility can be related to the position, shape and intensity of the reduction peaks of $H_2$-TPR curves[49]. The reduction peaks for each sample (Fig. 8) presented such differences which indicate that the catalyst reducibility is affected by the preparation method. Intense reduction peaks as well as the shifting of reduction peaks to lower temperatures were observed in the $H_2$-TPR profile of CWOH sample, indicating that this catalyst can be more reducible than CWOP one. Besides, the surface oxygen mobility increase can be associated with the decrease in the temperature at which the reduction peak appears. Mobile surface oxygen species can be easily removed under reduction atmosphere and higher mobility of surface oxygen ions helps in the removal of lattice oxygen during the reduction process[50]. This phenomenon could indicate that the amount of surface oxygen increases due to the diffusion of bulk oxygen to the surface. Thus, more bulk oxygen can be reduced resulting in more lattice oxygen involved in the oxidation for CWOH catalyst[49-52]. According to Sun et al.[53], the higher reducibility means the higher mobility of oxygen species in a catalyst. So, in this case, CWOH sample has the highest oxygen mobility. In addition, from Table 4, the consumption amount of hydrogen varies from $4.43x10^{-3}$ mol.gcat$^{-1}$ for CWOH, which was the most active catalyst, to $1.79x10^{-3}$ mol.gcat$^{-1}$ for CWOP, which was the less active catalyst. This result also indicates that the mobile oxygen species available on the CWOH surface are larger than that of CWOP[54]. The bulk and surface oxygen mobility play an important role in hydrocarbon oxidation reactions, in which the oxidation-reduction cycles determine the activity of the catalyst. The higher oxygen mobility facilitates the migration of oxygen species (that are consumed to oxidize toluene) across the catalyst structure, resulting in higher oxidation activity. Previous studies have demonstrated that toluene oxidation promoted by metal oxide catalysts follows the Mars-van Krevelen mechanism, in which the key steps are the supply of oxygen by the oxide, the introduction of the oxygen species from the lattice oxide into the substrate molecule and the re-oxidation of the reduced solid by the oxygen-containing gaseous phase, the rate-determining step of the reaction[51,55-58]. Thus, abundant mobility of active lattice oxygen species improves the catalytic activity in the toluene oxidation. Toluene oxidation promoted by $BaWO_4$ and $BaMoO_4$ catalysts was described in our previous paper in which we considered the role of oxygen mobility and oxygen vacancies in the process[14]. In the occasion, the $H_2$-TPR, $O_2$-chemisorption and EXAFS results indicated that $BaWO_4$ catalysts, compared with $BaMoO_4$ catalysts, had higher oxygen mobility and oxygen vacancies that appear to be the key factors for the achievement of better catalytic performances.
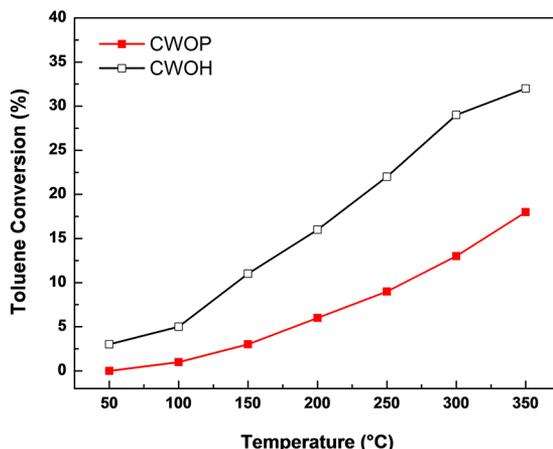


**Figure 9.** Gas-phase toluene conversion over $CaWO_4$ catalysts as a function of reaction temperature

## 4. Conclusions

In summary, $CaWO_4$ polycrystalline powders have been successfully synthesized by microwave-assisted hydrothermal method and by polymeric precursor method with scheelite-type tetragonal structure without secondary phase. Obtained particles have rounded and dumbbell-like morphology based on surfactant and polymeric agents under different experimental conditions. $N_2$ adsorption-desorption isotherms are of type III and exhibit a H3-type hysteresis loop. The optical band gap energy was calculated by the method proposed by Kubelka- Munk and the values obtained were about 5.2 eV. The PL emissions of these tungstates samples mainly attribute to the charge transfer within the $[WO_4]$ tetrahedron complex. Besides that, the powders prepared by MAH showed a higher PL emission intensity than powders prepared by PPM. The $H_2$-TPR results indicated that $CaWO_4$ sample prepared by MAH, compared with $CaWO_4$ sample prepared by PPM, have higher oxygen mobility that appear to be a key factor for the achievement of better catalytic performances.

## 5. Acknowledgments

## 6. References

1.  Zhang Y, Holzwarth NAW, Williams RT. Electronic band structures of the scheelite materials $CaMoO_4$, $CaWO_4$, $PbMoO_4$ and $PbWO_4$. *Physical Review B*. 1998;57(20):12738-12750.

Effect of Different Synthesis Methods on the Textural Properties of Calcium Tungstate (CaWO₄) and Its Catalytic Properties in the Toluene Oxidation

9

2. Gillette RH. Calcium and Cadmium Tungstate as Scintillation Counter Crystals for Gamma-Ray Detection. *Review Scientific Instruments*. 1950;21(4):294-301.

3. Oishi S, Hirao M. Growth of CaWO₄ whiskers from KCl flux. *Journal of Materials Science Letters*. 1989;8(12):1397-1398.

4. Nagirnyi V, Feldbach E, Jönsson L, Kirm M, Lushchik A, Lushchik C, et al. Excitonic and recombination processes in CaWO₄ and CdWO₄ scintillators under synchrotron irradiation. *Radiation Measurements*. 1998;29(3-4):247-250.

5. Xiang Y, Song J, Hu G, Liu Y. Synthesis of CaMoO₄ hierarchical structures via a simple slow-release co-precipitation method. *Applied Surface Science*. 2015;349:374-379.

6. Bourajoini H, Rautio AR, Kordas K, Mikkola JP. Calcium Manganese oxide catalysts for water oxidation: Unravelling the influence of various synthesis strategies. *Materials Research Bulletin*. 2016;79:133-137.

7. Watcharathamrongkul K, Jongsomjit B, Phisalaphong M. Calcium oxide based catalysts for ethanolysis of soybean oil. *Songklanakarin Journal of Science and Technology*. 2010;32(6):627-634.

8. Avramović JM, Veličković AV, Stamenković OS, Rajković KM, Milić PS, Veljković VB. Optimization of sunflower oil ethanolysis catalyzed by calcium oxide: RSM versus ANN-GA. *Energy Conversion and Management*. 2015;105:1149-1156.

9. Lang RJ, Neavel RC. Behaviour of calcium as steam gasification catalyst. *Fuel*. 1982;61(7):620-626.

10. De Lecea CSM, Almela-Alarcón MA, Linares-Solano A. Calcium-catalysed carbon gasification in CO₂ and steam. *Fuel*. 1990;69(1):21-27.

11. Cavalcante LS, Longo VM, Sczancoski JC, Almeida MAP, Batista AA, Varela JA, et al. Electronic structure, growth mechanism and photoluminescence of CaWO₄ crystals. *CrystEngComm*. 2012;14(3):853-868.

12. Gracia L, Longo VM, Cavalcante LS, Beltrán A, Avansí W, Li MS, et al. Presence of excited electronic state in CaWO₄ crystals provoked by tetrahedral distortion: An experimental and theoretical investigation. *Journal of Applied Physics*. 2011;110(4):043501.

13. Yu P, Bi J, Xiao DQ, Chen LP, Jin XL, Yang ZN. Preparation and microstructure of CaMoO₄ ceramic films prepared through electrochemical technique. *Journal of Electroceramics*. 2006;16(4):473-476.

14. Alencar LDS, Mesquita A, Feitosa CAC, Balzer R, Probst LFD, Batalha DC, et al. Preparation, characterization and catalytic application of Barium molybdate (BaMoO₄) and Barium tungstate (BaWO₄) in the gas-phase oxidation of toluene. *Ceramics International*. 2017;43(5):4462-4469.

15. Maurera MAMA, Souza AG, Soledade LEB, Pontes FM, Longo E, Leite ER, et al. Microstructural and optical characterization of CaWO₄ and SrWO₄ thin films prepared by a chemical solution method. *Materials Letters*. 2004;58(5):727-732.

16. Wilson GJ, Matijasevich AS, Mitchell DRG, Shulz JC, Will GD. Modification of TiO₂ for Enhanced Surface Properties: Finite Ostwald Ripening by a Microwave Hydrothermal Process. *Langmuir*. 2006;22(5):2016-2027.

17. Huang H, Xu Y, Feng Q, Leung DYC. Low temperature catalytic oxidation of volatile organic compounds: a review. *Catalysis Science and Technology*. 2015;5(5):2649-2669.

18. Bilecka I, Niederberger M. Microwave chemistry for inorganic nanomaterials synthesis. *Nanoscale*. 2010;2(8):1358-1374.

19. Li WB, Wang JX, Gong H. Catalytic combustion of VOCs on non-noble metal catalysts. *Catalysis Today*. 2009;148(1-2):81-87.

20. Liotta LF. Catalytic oxidation of volatile organic compounds on supported noble metals. *Applied Catalysis B:Environmental*. 2010;100(3-4):403-412.

21. Kamal MS, Razzak SA, Hossain MM. Catalytic oxidation of volatile organic compounds (VOCs) - A review. *Atmospheric Environment*. 2016;140:117-134.

22. Michalowicz A, Moscovici J, Muller-Bouvet D, Provost K. MAX: Multiplatform applications for XAS. *Journal of Physics: Conference Series*. 2009;190(1):012034.

23. Ankudinov AL, Ravel B, Rehr JJ, Conradson SD. Real-space multiple-scattering calculation and interpretation of x-ray-absorption near-edge structure. *Physical Review B*. 1998;58(12):7565-7576.

24. Cullity DB. *Elements of X-ray Diffraction*. Reading: Addison-Wesley; 1956.

25. Thongtem T, Kungwankunakorn S, Kuntalue B, Phuruangrat A, Thongtem S. Luminescence and absorbance of highly crystalline CaMoO₄, SrMoO₄, CaWO₄ and SrWO₄ nanoparticles synthesized by co-precipitation method at room temperature. *Journal of Alloys and Compounds*. 2010;506(1):475-481.

26. Yang Y, Wang X, Liu B. Synthesis of CaWO₄ and CaWO₄:Eu microspheres by precipitation. *Nano*. 2014;9(1):1450008.

27. Su Y, Li G, Xue Y, Li L. Tunable Physical Properties of CaWO₄ Nanocrystals via Particle Size Control. *Journal of Physical Chemistry C*. 2007;111(18):6684-6689.

28. Sen A, Pramanik P. A chemical synthetic route for the preparation of fine-grained metal tungstate powders (M=Ca, Co, Ni, Cu, Zn). *Journal of the European Ceramic Society*. 2001;21(6):745-750.

29. Ryu JH, Yoon JW, Lim CS, Oh WC, Shim KB. Microwave-assisted synthesis of nanocrystalline MWO₄ (M: Ca, Ni) via water-based citrate complex precursor. *Ceramics International*. 2005;31(6):883-888.

30. Chen Z, Gong Q, Zhu J, Yuan YP, Qian LW, Qian XF. Controllable synthesis of hierarchial nanostructures of CaWO₄ and SrWO₄ via facile low-temperature route. *Materials Research Bulletin*. 2009;44(1):45-50.

31. Thongtem T, Phuruangrat A, Thongtem S. Synthesis of CaWO₄, SrWO₄ and BaWO₄ with nanosized particles using cyclic microwave radiation. *Journal of Ceramic Processing Research*. 2008;9(3):258-261.

32. Wang G, Lin S, Wan G. Growth Process and Optical Properties of SrWO₄ Microcrystal Prepared by a Microwave-Assisted Method. *Synthesis and Reactivity in Inorganic, Metal-Organic, and Nano-Metal Chemistry*. 2012;42(6):888-891.

33. Zhang L, Dai JS, Lian L, Liu Y. Dumbbell-like BaWO₄ microstructures: Surfactant-free hydrothermal synthesis, growth mechanism and photoluminescence property. *Superlattices and Microstructures*. 2013;54:87-95.

34. Li YF, Ouyang JH, Zhou Y, Liang XS, Murakami T, Sasaki S. Room-temperature template-free synthesis of dumbbell-like SrSO4 with hierarchical architecture. *Journal of Crystal Growth*. 2010;312(11):1886-1890.

35. Gregg SJ, Sing KSW. *Adsorption, Surface Area and Porosity*. London: Academic Press; 1967.

36. Escobedo Morales A, Sánchez Mora E, Pal U. Use of diffuse reflectance spectroscopy for optical characterization of un-supported nanostructures. *Revista Mexicana de Física*. 2007;53(5):18-22.

37. Vieira EG, Sousa PAA, Matos JME, Santos MRMC. Síntese pelo método da coprecipitação e caracterização estrutural do tungstato de cálcio com estrutura tipo scheelita. *Cerâmica*. 2013;59(351):417-425.

38. Ghoreishi SM. Facile synthesis and characterization of CaWO₄ nanoparticles using a new Schiff base as capping agent: enhanced photocatalytic degradation of methyl orange. *Journal of Materials Science: Materials in Electronics*. 2017;28(19):14833-14838.

39. Campos AB, Simões AZ, Longo E, Varela JA, Longo VM, Figueiredo AT, et al. Mechanisms behind blue, green, and red photoluminescence emissions in CaWO₄ and CaMoO₄ powders. *Applied Physics Letters*. 2007;91(5):051923.

40. Bakovets VV, Yushina IV, Antonova OV, Zolotova ES. Bandgap-width correction for luminophores CaMoO₄ and CaWO₄. *Optics and Spectroscopy*. 2017;123(3):399-403.

41. Longo VM, Cavalcante LS, Paris EC, Sczancoski JC, Pizani PS, Siu-Li M, et al. Hierarchial Assembly of CaMoO₄ Nano-Octahedrons and their Photoluminescence Properties. *Journal of Physical Chemistry C*. 2011;115(13):5207-5219.

42. Perales RL, Fuertes JR, Errandonea D, Garcia DM, Segura A. Optical absorption of divalent metal tungstates: Correlation between the band-gap energy and the cation ionic radius. *EPL*. 2008;83(3):37002.

43. Tablero C. Optical absorption and applications of the ABO₄ (A = Ca, Pb and B = Mo, W) semiconductors. *Chemical Physics Letters*. 2015;635:190-195.

44. Marques VS, Cavalcante LS, Sczancoski JC, Alcântara AFP, Orlandi MO, Moraes E, et al. Effect of Different Solvent Ratios (Water/Ethylene Glycol) on the Growth Process of CaMoO₄ Crystals and Their Optical Properties. *Crystal Growth & Design*. 2010;10(11):4752-4768.

45. Zhang Y, Wang L, Chu D, Wang L, Wang Z, Wang Z. Controllable synthesis and luminescent properties of hierarchical flowerlike CaMoO₄ microspheres. *Nano-Structures & Nano-Objects*. 2016;6:46-51.

46. Rocca F, Kuzmin A, Mustarelli P, Tomasi C, Magistris A. XANES and EXAFS at Mo K-edge in (AgI)₁₋ₓ(AgMoO₄)ₓ glasses and crystals. *Solid State Ionics*. 1999;121:189-192.

47. Report on the International Workshops on Standards and Criteria in XAFS. In: Hasnain SS, ed. *X-ray Absorption Fine Structure*. York: Ellis Horwood; 1991.

48. Curcio AL, Bernardi MIB, Mesquita A. Local structure and photoluminescence properties of nanostructured Zn₁₋ₓMnₓS Material. *Physica Status Solidi C*. 2015;12(12):1367-1371.

49. Silva AGM, Rodrigues TS, Dias A, Fajardo HV, Gonçalves RF, Godinho M, et al. Ce₁₋ₓSmₓO₁.₉₋δ nanoparticles obtained by microwave-assisted hydrothermal processing: an efficient application for catalytic oxidation of α-bisabolol. *Catalysis Science and Technology*. 2014;4(3):814-821.

50. Rao GR, Mishra BG. Structural, redox and catalytic chemistry of ceria based materials. *Bulletin of the Catalysis Society of India*. 2003;2:122-134.

51. Liu P, He H, Wei G, Liu D, Liang X, Chen T, et al. An efficient catalyst of manganese supported on diatomite for toluene oxidation: Manganese species, catalytic performance, and structure-activity relationship. *Microporous and Mesoporous Materials*. 2017;239:101-110.

52. Sihaib Z, Puleo F, Garcia-Vargas JM, Retailleau L, Descorme C, Liotta LF, et al. Manganese oxide-based catalysts for toluene oxidation. *Applied Catalysis B: Environmental*. 2017;209:689-700.

53. Sun M, Lan B, Yu L, Ye F, Song W, He J, et al. Manganese oxides with different crystalline structures: Facile hydrothermal synthesis and catalytic activities. *Materials Letters*. 2012;86:18-20.

54. Sun GB, Hidajat K, Wu XS, Kawi S. A crucial role of surface oxygen mobility on nanocrystalline Y₂O₃ support for oxidative steam reforming of ethanol to hydrogen over Ni/Y₂O₃ catalysts. *Applied Catalysis B: Environmental*. 2008;81(3-4):303-312.

55. Doornkamp C, Ponec V. The universal character of the Mars and Van Krevelen mechanism. *Journal of Molecular Catalysis A: Chemical*. 2000;162(1-2):19-32.

56. Qu Z, Bu Y, Qin Y, Wang Y, Fu Q. The improved reactivity of manganese catalysts by Ag in catalytic oxidation of toluene. *Applied Catalysis B: Environmental*. 2013;132-133:353-362.

57. Liu Y, Dai H, Deng J, Xie S, Yang H, Tan W, et al. Mesoporous Co₃O₄-supported gold nanocatalysts: Highly active for the oxidation of carbon monoxide, benzene, toluene, and o-xylene. *Journal of Catalysis*. 2014;309:408-418.

58. Gómez DM, Galvita VV, Gatica JM, Vidal H, Marin GB. TAP study of toluene total oxidation over Co₃O₄/La-CeO₂ catalyst with an application as a washcoat of cordierite honeycomb monoliths. *Physical Chemistry Chemical Physics*. 2014;16(23):11447-11455.